RSC Advances

PAPER

View Article Online
View Journal | View Issue

Cite this: *RSC Adv.*, 2020, **10**, 16551

A study of deactivation by H_2S and regeneration of a Ni catalyst supported on Al_2O_3, during methanation of CO_2. Effect of the promoters Co, Cr, Fe and Mo†

David Méndez-Mateos, V. Laura Barrio,* Jesús M. Requies and José F. Cambra

Energy storage from renewable sources is possible by chemical procedures, power to gas technology being a possible solution for long-term storage. In this work, CO_2 methanation from a sulphur containing gas was studied, taking into account deactivation of the catalysts and a regeneration process. In order to improve the sulphur resistance of a standard nickel (13%) catalyst supported on alumina, transition metals like molybdenum (Mo), iron (Fe), cobalt (Co) or chromium (Cr), in different proportions (from 4 to 8 wt%) were added to the catalyst formulation. The catalyst activity, between 573 and 773 K, at 10 bar, increased when transition metals were added except for Mo in the highest proportion. These bimetallic catalysts presented a similar deactivation resistance than the monometallic catalyst when sulphur was present in the feed. Once H_2S was removed from the feed, and the catalysts regenerated with oxygen, only the catalyst containing cobalt recovered up to a 13% methane yield.

Received 29th January 2020
Accepted 4th April 2020

DOI: 10.1039/d0ra00882f

rsc.li/rsc-advances

1. Introduction

Energy strategies in the EU have faced very important transformations after the decision about the 2030 climate and energy package.[1] Some of the energetic strategies of this program are the emission reduction from fossil fuels, replacing conventional with renewable energy sources and searching for new and more efficient processes to harness the available sources, reducing the greenhouse gases in Earth's atmosphere.[2] Renewable systems produce clean energy from sun, wind or water which are available natural resources.[3] However, the energy production depends on the availability and quantity of the natural resources, and may cause temporal and spatial energy fluctuations in the grid. That could be solved by energy storing when the supply exceeds the demand and using it when the demand is larger than the supply. Nowadays the energy storage systems are varied, with different advantages and disadvantages. Depending on the application the requirement about efficiency, self-discharge rate, rapid-response, lifetime, life cycle, capital cost, technology maturity or resources decide the appropriate system.[4–6] On the other hand what is clear is that in this transition to a system based on renewable energies a combination of all them would be necessary. In the case of the long-term energy storage the power-to-gas technology present some advantages converting renewable power to fuel or chemicals. Some of the main advantages of power-to-gas (PtG) technology are: continuously decreasing production cost due to the advances in electrolysis technology, availability of low-cost electricity, long-term energy storage, recycled or captured CO_2 is needed and large amount of energy/electricity is stored.

Power-to-gas is a technology which converts the excess electricity into a gaseous fuel, such as hydrogen or methane in two steps (Fig. 1), and it is supporting the penetration of the renewable sources.[7]

In the first step, hydrogen and oxygen are produced *via* water electrolysis (eqn (1)). Oxygen can be released to the atmosphere or used as raw material in industrial production process, but the main product of this transformation is hydrogen like fuel (whose burn product is water);[8] then it can be transported or stored either in a dedicated distribution grid or mixed in the existing natural gas infrastructure.[9]

$$H_2O \rightarrow H_2 + \frac{1}{2}O_2 \quad (1)$$

In a second step, methane is produced *via* carbon dioxide hydrogenation (methanation), using the hydrogen from the first step, process known as Sabatier reaction (eqn (2)). This reaction has been extensively studied and applied industrially since 1900s, using catalysts based on nickel, ruthenium, rhodium and cobalt as active metals and alumina as support for the

School of Engineering (UPV/EHU), Plaza Ingeniero Torres Quevedo 1, Bilbao 48013, Spain. E-mail: laura.barrio@ehu.eus

† Electronic supplementary information (ESI) available. See DOI: 10.1039/d0ra00882f

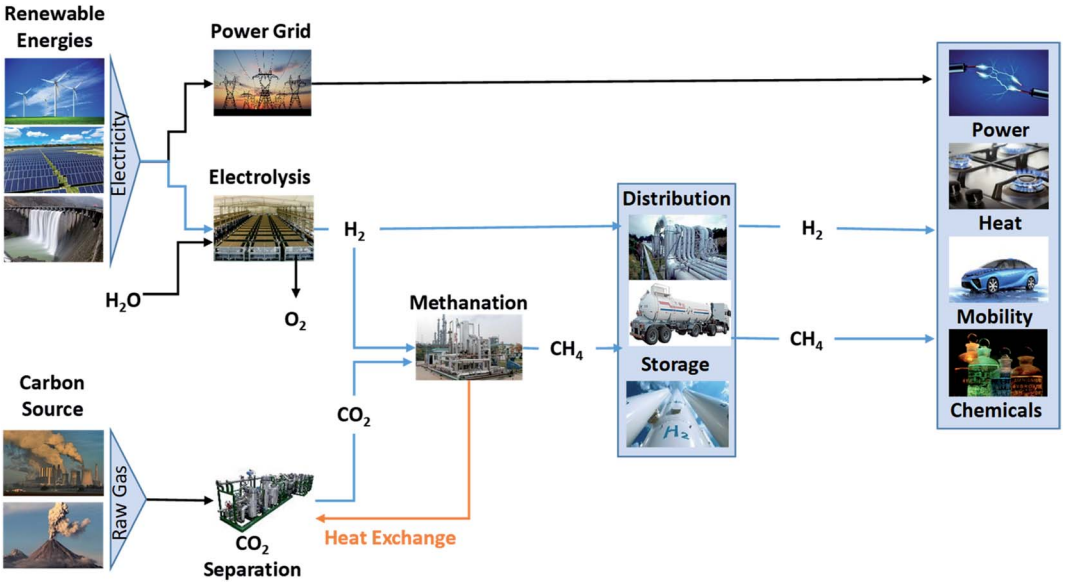

Fig. 1 Scheme of power-to-gas technology.

catalyst, being Ru–Al_2O_3 catalyst one of the most active systems.[8] The carbon dioxide could be obtained from exhaust or process gases of industrial processes or fossil power plants, biogas plants or from the atmosphere. The methane produced can be stored, burned or injected into the existing natural gas grid, being cheaper and easier than for the hydrogen.[10]

$$CO_2 + 4H_2 \rightleftarrows 2H_2O + CH_4 \quad \Delta H_{298\ K} = -165\ kJ\ mol^{-1} \quad (2)$$

The carbon dioxide from biogas industry is a good source and when biogas is produced large amounts of carbon dioxide are generated but with the problem of the presence of other compounds, that are deleterious for the catalyst performance. The usual biogas composition is 50–75% CH_4, 50–25% CO_2, 0–10% N_2 and 0–3% H_2S.[11] One of the major challenges in utilizing biogas is the presence of H_2S as the catalyst deactivates by sulphur poisoning.[12,13]

This research was planned to improve the methanation step of the PtG process, based on Sabatier reaction, employing renewable H_2 and CO_2 from biogas, which contains hydrogen sulphide. The nickel, ruthenium, rhodium, platinum and palladium catalysts have been wide reported as active catalyst in Sabatier reaction, supported on different metal oxides (CeO_2 or Al_2O_3, among others) due to the high available area.[14–18] The high surface, stability, activity and selectivity improved on metallic catalyst due to γ-Al_2O_3 structure, specially, at operation conditions, marking this support how most suitable.[13,19] Moon *et al.*[14] combined Ni, Ce and Zr to store oxygen achieving 82% CO_2 conversion at 573 K and atmospheric pressure.

The low price and the good activity of the nickel with respect to noble metals, implied all of the catalysts prepared were based on nickel as active metal.[20–22] Addition of transition metals increased the dispersion and the reducibility of the nickel species, same effect than using noble metals but with significantly lower price.[20,21] The nickel species provide high activity in Sabatier reaction, but high sulphur sensitivity, it was necessary the addition of modifier that doped the metal surface. The transition metals used were VIIIB metals, mainly Co, Cr, Mo or Fe because of contribute the H_2S resistance of the catalyst.[23–27]

There are limited reports that investigate the H_2S effect in the catalyst deactivation in methanation reaction, being studied in other processes like the steam reforming or water gas shift (WGS). Zhang *et al.*,[28] studied the deactivation in the WGS reaction to design Fe-based sulphur tolerant catalyst in which sulphur-related phases were not observed. In this work, the authors explained that the tolerance of H_2S to metal, thus chemical bonding, block or inhibit active sites and this could cause a marked activity loss specially for the Cu samples. Generally the deactivation of transition metal catalysts in the presence of H_2S is an exponential function of time, described by Appari *et al.*,[11] and takes from 5 to 20 h in the case of the steam reforming system to complete deactivation. Ni catalyst supported on γ-Al_2O_3 was studied in this work for the deactivation and regeneration as a function of concentration of H_2S and the temperature. The sulphur removal and Ni-based catalyst regeneration was widely studied by Li *et al.*,[29] focused on sulphur removal in the form of SO_2 from a biomass derived syngas. Feng *et al.*[30] studied the regeneration of the catalyst removing the catalyst poison over iron oxide employing N_2-diluted air (6 vol% O_2) achieving high desulphurization and regeneration yield after many sulphidation–regeneration cycles.

In the present work, Ni was chosen as the active metal due to its low price with respect to platinum group metals, while maintaining a good activity.[11] In order to improve the catalyst performance, the effect of transition metals such as Co, Cr, Fe and Mo was studied in order to improve active metal dispersion, reducibility and, probably, catalyst resistance to H_2S poisoning.[23,25,26,31–33] The catalysts were supported on γ-Al_2O_3 and prepared by the incipient impregnation method, which facilitates the dispersion of the metals on the support, and their

interaction.[27,34] The H_2S effect and resistance over catalyst activity and the regeneration capability by different ways.

2. Experimental details

2.1. Catalyst preparation

The bimetallic catalyst supported on γ-Al_2O_3 (Alfa-Aesar) were synthesized by incipient wetness impregnation method. The metallic precursors employed for catalysts preparation were the following:

- Nickel(II) nitrate hexahydrate (99.999 wt%, Sigma Aldrich).
- Iron(III) chloride hexahydrate (97 wt%, PRS Panreac Química).
- Chromium(III) nitrate nonahydrate (98.5 wt%, Alfa Aesar).
- Cobalt(II) chloride hexahydrate (99 wt%, Quimivita S.A.).
- Ammonium heptamolybdate tetrahydrate (99 wt%, Merck).

Measured quantities of support γ-Al_2O_3 (5 g) and metal precursors in order to achieve the desired metal loading (13 wt% Ni and 4 wt% Co, 4 wt% Cr, 4 wt% Fe, 4 wt% Mo or 8 wt% Mo) were mixed and then dissolved in distilled water. A volume equal to or slightly in excess of the total pore volume calculated for the support was used, being 20 ml in the case of alumina. The optimal pH value was related with the isoelectric point (icp), when the zeta potential is zero (pzc), achieving that when the net charge on the surface is zero. The pzc of gamma alumina powder was found to be pH 7.5. For the pH value over pzc, the support has high affinity for protons and thus remains positively charged up to high pH values.[19,35] The solution was stirred continuously measuring the pH, to achieve a pH of 8.5 adding ammonium (Panreac) to increase the pH or nitric acid (Scharlau) to decrease the pH value. At pH 8.5, the solution was stirred overnight, in order to ensure homogeneous mixture during the impregnation process and to avoid the formation and precipitation of metal hydroxides of ref. 36, not detected during the preparation process of the catalysts in this work. In a rotary evaporator (Heidolph Laborota 4000) was evaporated the solvent to dryness, helped for a vacuum pump that reduce the boiling point of the solution. The solvent evaporation was attained, heating at 338 K, and reducing slowly the pressure until 40–100 mbar.

Once the solvent was evaporated, the solid so obtained was introduced in an oven at 373 K during 2 h in order to ensure a complete drying. After that, the sample was calcined at 673 K (to ensure the stability of the γ-Al_2O_3) in presence of air for 2 h, with a ramp of 1 K min^{-1}. Finally, the calcined catalysts were pressed and sieved to the desired particle size: 0.42 mm < d_p < 0.50 mm. It was chosen this particle size (d_p) in order to avoid reagents bypassing near the wall according to an internal pipe diameter-to-particle size ratio higher than 10.[37]

The catalysts prepared were named, according to their nominal composition, as follows: 4Co–13Ni/Al_2O_3, 4Cr–13Ni/Al_2O_3, 4Fe–13Ni/Al_2O_3, 4Mo–13Ni/Al_2O_3 and 8Mo–13Ni/Al_2O_3.

2.2. Catalyst characterization

The main techniques employed to determine the physico-chemical properties of the catalysts were: temperature-programmed reduction (TPR), inductively coupled plasma-optical emission spectroscopy (ICP-OES), N_2 adsorption–desorption isotherms at 77 K, X-ray photoelectron spectroscopy and X-ray diffraction.

2.2.1 TPR. Reducible species present in the catalysts and their reduction temperatures were determined. The equipment used was an Autochem, equipped with a thermal conductivity detector. It was loaded with approximately 0.05 g of fresh catalysts powder an U shaped quartz tube and heated from room temperature to 473 K for 1 h in Ar stream (30 ml min^{-1}). The samples were then cooled down to 323 K and the Ar was replaced by 5 vol%, H_2/Ar (45 ml min^{-1}) stream. The samples were heated from 323 K to 973 K, at a ramp rate of 10 K min^{-1}.

2.2.2 TPD. The NH_3-TPD and CO_2-TPD profiles were determined employing the Autochem, the acid and basic centres of the catalysts were analysed according to the NH_3 or CO_2 desorbed per unit time and catalyst mass. Depending on the quantity of NH_3 or CO_2 desorbed and the temperature of desorption, the acid strength and concentration were determined.

2.2.3 ICP-OES. The equipment employed for this analysis was a PerkinElmer Optima 3300DV. The Ni, Co, Cr, Fe and Mo contents in the catalysts were measured. The solid samples were firstly disaggregated in acid solution (mixture of 3 : 1 HCl and HNO_3 respectively), and then analysed.

2.2.4 N_2 adsorption–desorption isotherms. The textural properties (BET surface area, pore size distribution and average pore diameter) of the catalysts were determined using an Autosorb 1C-TCD. In order to remove the moisture and any adsorbed gases, the samples were degassed under vacuum at 573 K during 3 h.

2.2.5 XPS. To determine the elemental composition at the surface of the catalysts. The equipment employed was a SPECS (Berlin, Germany) system equipped with a Phoibos 150 1D-DLD analyser and an Al Kα (1486.6 eV) monochromatic radiation source with electrons output angle of 90° to obtain XPS patterns of reduced and used catalyst. XPS is a technique that allows the study of the species present on the surface of the catalyst and their chemical state.

2.2.6 XRD. The analysis was conducted for catalyst samples between $2\theta = 20°$ to 90° using CuK_α radiation ($\lambda = 0.15418$ nm) at 40 kV and 30 mA, calculating crystalline species and an approximation of the average crystal size. X-ray diffraction patterns were obtained using a PANalytical X'Pert Pro diffractometer. Preceding the analysis, samples were reduced at 1073 K during 4 h. XRD technique can measure at about 1–2 μm depth of the sample. It was used Scherrer equation (3) to calculate the average particle size of the crystalline species.

$$d = K\lambda/B(2\theta)\cos\theta \quad (3)$$

where is the shape factor (0.89), λ is the X-ray wavelength, $B(2\theta)$ is the line broadening at half the maximum intensity in radians, and θ is the Bragg angle.[38]

2.2.7 SEM and TEM. The fresh and used samples were analysed by TEM (Transmission Electron Microscopy) and by SEM (Scanning Electron Microscopy), determining the morphology of the active phase of fresh and used with H_2S catalysts. The measurements were carried out employing a Philips CM200 transmission electron microscopy with resolution of 137 eV and

the JEOL JSM-7000F scanning electron microscopy with resolution until 1.2 nm (mode secondary electrons and 30 kV) and detector EDX INCA X-sight Serie Si (Li) pentaFET Oxford.

2.3. Activity test

To study the catalyst activity a bench-scale plant was used (PID Eng&Tech), where it 0.2 g of catalyst were introduced in a stainless steel fixed bed reactor. The catalyst was diluted with inert SiC, in order to minimize thermal gradients in the catalytic bed ($\text{weight}_{\text{catalyst}}/\text{weight}_{\text{SiC}} = 1:4.5$). The reactor employed had 0.635 cm inner diameter and 32 cm of length, placing the catalyst in the central zone to an effective heating in an electrical furnace. Furnace temperature was adjusted to maintain the catalyst bed under isothermal condition, using two thermocouples: the first one inside the catalytic bed to measure the reactor temperature, and the second one before the catalytic bed in order to control the inlet temperature accurate. The first step was the catalyst activation, reducing the catalyst with a mixture of N_2 (99.999%) and H_2 (99.999%) with a ratio of H_2/N_2 equal to 3 : 1 (65 N ml min^{-1} of H_2) at 673 K during 4 h. Once the catalyst was activated, the reaction gasses, H_2 and CO_2, were fed in a ratio H_2/CO_2 of 4 : 1. Thus is the stoichiometry proportion for the methanation reaction to obtain biogas (eqn (4)). The methanation reaction is the combination of eqn (5) and (6), in which the CO could be generated as an intermediate product, or as a final product in combination with methane, in case the reactions of eqn (4) and (5) run parallel to each other.[21] The weight hourly space velocity of the flow fed was 33.5 g_{feed} $(g_{\text{cat}}\ \text{h})^{-1}$.

$$CO_2 + 4H_2 \rightleftarrows CH_4 + 2H_2O \quad (4)$$

$$CO_2 + H_2 \rightleftarrows CO + H_2O \quad (5)$$

$$CO + 3H_2 \rightleftarrows CH_4 + H_2O \quad (6)$$

A schematic representation of the system is shown in Fig. S1.† The reactor was heated to the desired temperature at a rate of 10 K min^{-1} under N_2 flow and the catalyst activity was studied at different temperatures, between 573 K and 773 K, and at 10 bar of pressure, separating the reaction products in a Peltier condenser: condensed water and gas products. Each 10 min the output massflow and composition of the gases were analysed, maintaining each temperature 60 min, corresponding with 6 points, collecting the water produced, weighing and measuring in this time. The gas phase composition was on-line analysed using a Varian CP-4900 MicroGC equipped with a high sensitivity TCD and two columns (10 m molecular sieve 5, 10 m Poraplot Q).

For a better understanding of the process, the parameter used in the calculations were calculated, which are defined below:

$$\text{CH}_4\ \text{yield: } \eta_{\text{CH}_4} = \text{mol } \text{CH}_4^{\text{out}}/\text{mol } \text{CH}_4^{\text{out}}\ \text{stoichiometric} \times 100 \quad (7)$$

$$\text{TOF}\left(\text{h}^{-1}\right) = \frac{[\text{CO}_2]_{\text{in}} X_{\text{CO}_2}}{Dn} \quad (8)$$

$$D = \frac{6\text{M}_{\text{Ni}}}{dA_{\text{Ni}}\rho_{\text{Ni}}N_{\text{Avogadro}}} \quad (9)$$

where $[CO_2]_{\text{in}}$ refer to inlet CO_2 stream, X_{CO_2} is the CO_2 fractional conversion, n is the molar Ni (as determined by ICP), D is the Ni dispersion (surface metal per total metal atoms),[39] M_{Ni} is the Ni atom mass, d is the Ni particle diameter (obtained from STEM measurements), A_{Ni} is the Ni atom surface area, ρ_{Ni} is the Ni density and N_{Avogadro} is the Avogadro number.

Once the activity of the bimetallic catalyst was tested in the methanation reaction from biogas flow, the next step was the reaction with a sulphur containing biogas (50 ppm H_2S, 20 vol% CO_2 and 80 vol% H_2). The methanation reactions were continued in the presence of H_2S until catalyst deactivation. Two different techniques have been explored for catalyst regeneration

- Removal of H_2S from feed stream

- Catalyst treatment with an O_2 mixture flow (200 N ml min^{-1} N_2 and 10 N ml min^{-1} O_2) at 773 K during 4 h, and reducing the catalyst with a mixture of N_2 and H_2 in a 3 : 1 (65 : 195 N ml min^{-1}) ratio at 673 K during 4 h.

The active catalyst, regenerated, was used again in methanation reaction of H_2 and CO_2 with 4 : 1 ratio at 773 K and 10 bar to measure the regeneration effectiveness and the H_2S resistance of the catalyst.

All the experiments were repeated to ensure reproducibility.

3. Results and discussion

3.1. Catalyst characterization

3.1.1 ICP analysis. The metal composition of the catalyst was measured by ICP-OES analysis, determining the iron, cobalt, chromium, molybdenum and nickel content. All catalysts were prepared to obtain a nominal content of 13 wt% of Ni and 4 wt% of promoter metal. An additional sample containing an 8 wt% of Mo was prepared. As shown in Table 1, the actual metal content of the catalysts were close to the theoretical, being the highest deviations present in the Ni and Co–Ni catalysts.

3.1.2 BET measurements. The textural properties of supports and prepared catalysts were analysed in an Autosorb 1C-TCD, measuring the N_2 adsorption and desorption isotherms obtain summarized in Table 1. The isotherms obtained are type-IV, exhibiting H2 hysteresis loops, due to the presence of "ink-bottle" mesoporous structure.[40] The main textural properties studied were surface area, average pore diameter and pore volume (Table 1). These properties were compared for the different calcined catalyst with respect to the calcined support (γ-Al_2O_3) to determine the effect of the metal addition over the support. The surface area of the support (202 $m^2\ g^{-1}$) was reduced slightly with the nickel addition (180 $m^2\ g^{-1}$) due to the nickel deposition into the support channels, attached inside the mesopore, and partially blocking its internal pore volume during the impregnation step.[41] The addition of a second metal resulted in lower surface area and pore volume, as after the metal incorporation channels and pores of the support can be blocked. But for the cobalt–nickel bimetallic

Table 1 Metal content in prepared catalysts measured by ICP-OES

	Composition (wt%)							
Sample	X[a]	Ni	S_{BET}[b] ($m^2\ g^{-1}$)	V_P[c] ($m^3\ g^{-1}$)	D_P[d] (nm)	D^{e1}_{XRD} (nm)	D^{e2}_{XRD} (nm)	TOF_{CO_2}[f] (h^{-1})
Al_2O_3	—	—	202	0.81	7.7	—	—	—
$13Ni/Al_2O_3$	—	13.9	180	0.55	7.2	5	10	2951
$4Co–13Ni/Al_2O_3$	4.5	12.5	187	0.22	5.1	5	10	784
$4Cr–13Ni/Al_2O_3$	3.8	13.2	179	0.26	6.2	5	10	1676
$4Fe–13Ni/Al_2O_3$	4.0	13.0	115	0.17	6.3	5	10	2958
$4Mo–13Ni/Al_2O_3$	4.2	12.8	101	0.15	6.2	5	10	2745
$8Mo–13Ni/Al_2O_3$	8.2	12.8	108	0.16	6.4	5	10	2301
Commercial	—	12.4	22	0.09	16.9	—	—	—

[a] Metal promoter (Co, Cr, Fe or Mo) according to the corresponding catalyst. [b] The surface area was calculated by the BET equation. [c] BJH desorption pore volume. [d] BJH desorption average pore diameter. [e] D^{e1}_{XRD} (after reduction) and D^{e2}_{XRD} (after reaction) are an approximation calculated from Ni (111) plane using Scherrer equation. [f] TOF_{CO_2} were calculated from eqn (8) reaction conditions: GHSV = 36 000 h^{-1}, T = 683 K, at 1 atm.

catalyst, the surface area slightly increased in relation to nickel monometallic catalyst. In the case of Fe, this decrease can be attributed to the destruction of mesopores structure or pore blockage.[42] And similar trend for the Mo, as a higher amount of metal was incorporated, was observed.[43]

3.1.3 H_2-TPR studies. The H_2-TPR profiles of the different Ni catalysts in Al_2O_3 supported and calcined at 673 K, are collected in Fig. 2. According to the bibliography,[44] a correlation is stablished between temperature and nature of reduction peaks. Usually, peaks under 873 K are assigned to NiO species with low to moderate interaction with the support and over these values, with non-stoichiometric and stoichiometric nickel aluminate, not being detected in the analyzed catalysts. This is due to an interesting outcome of this work is that the addition of the second metal decreased the reduction temperature under 750 K, lower than the maximum temperature in activity tests. Depending of the metal, the number and the position of the reduction peaks are different, corresponding to the reduction of different species (NiO–Al, $NiAl_xO_y$,…). In the work of Rynkowski *et al.*[44] the effect of Ru and Ni in systems supported over Al_2O_3 in the different characterization analysis was studied. The addition of a second metal, in this case a noble metal, leads to decrease the reduction temperature, approaching the Ni reduction peak to Ru reduction peak, splitting in two peaks for proportions of Ru higher than 15%, effect of the higher contribution of RuO than NiO, as the effect observed in these experiments.

In the case of Co, the peak appeared at around 605 K; and for the Fe catalyst two similar peaks were measured at 520 K and at 582 K, all of them attributed to nickel oxide species with a weak interaction with the support. In the case of the iron, some Fe_2O_3 was measured by XRD, as the reduction of Fe_2O_3 to Fe_3O_4 normally occurs between 533–643 K, some reduction of Fe_2O_3 could happen overlapped by the nickel oxide reduction.[45] Thus, by the addition of Co and Fe, the reduction peaks clearly shifted to lower temperature indicating a weaker interaction of Ni with the support.

The addition of Cr showed a small and narrow peak at a low temperature (486 K) and another wider from 550 K until 750 K approximately. But there is not a significant peak for the nickel reduction and this profile can be attributed to NiO species with low interactions. For the Mo–Ni catalysts with content 4 : 13 and 8 : 13, a peak at 660 K and two shoulders (at 500 K and 720 K approximately) were observed.

For the Mo catalyst, the reduction of Mo^{6+} to Mo^{4+} appeared at temperatures around 748 K as the peaks appeared in the range between 600 K and 700 K only the reduction of NiO species are observed with weak interaction at the lower

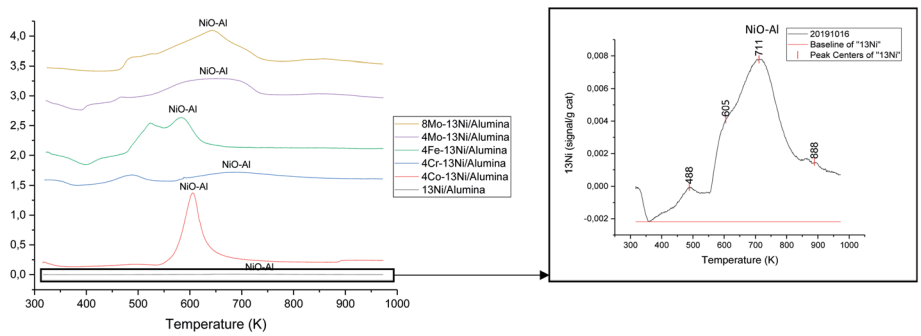

Fig. 2 H_2-TPR profiles of the prepared catalysts in 4% H_2/Ar atmosphere and 10 K min^{-1} heating rate.

temperature (623 K) and with stronger interaction at the higher temperature (880 K).[46] But for all the bimetallic catalysts the presence of nickel aluminate species was not measured as they appear at temperatures higher than 1173 K, and this peak was not detected (Fig. 3).

In general, the addition of metal promoters (Co, Cr, Fe and Mo) facilitates the reducibility of the catalyst. The promoters interact with the metal (Ni) achieving a higher degree of reducibility that could promote the NiO dispersion and decrease their particle size.

3.1.4 TPD studies. In order to determine the quantity and strength of catalyst acid and basic sites, the NH_3 and CO_2 previously bonded to acid and basic centres respectively were desorbed. Desorption temperature determines the strength of the bond, so that higher desorption temperature means stronger bond.

The NH_3-TPD profiles are slightly different according to metal added to nickel–alumina, increasing or decreasing the desorption temperature to which weak and strong acid centres desorbed NH_3. These profiles are shown in Fig. 4. The main peaks are shown at *ca.* 547 K, 597 K, 808 K and 1.073 K, corresponding to weak acid sites the first and second one and to strong acid sites the other two.[47,48] The amount of acid centres, and their distribution, related to ammonia desorption, are presented in Table 3 for the studied range. The medium acid sites of alumina are coordinated with NH_3, due to the electron deficiency of trivalent aluminium atoms, presenting a maximum centred at 548 K.[48] Furthermore, the peak centred at 1.073 K, in strong acid region, could corresponds with Brønsted acid sites by the hydrogen atoms that may act as proton donor,[49] presenting more amount for all the catalysts studied.

As can be observed in Table 3, all the bimetallic catalysts presented a higher acidity than the base catalyst, especially for medium acid sites. Only the catalyst with Cr as promoter presented qualitatively a lower acidity, probably due to CrO_3 partial reduction to Cr_2O_3. However, the different oxidation states that Cr can be present (with valences from 2 to 6), and facilitate a higher incorporation of acid centres, especially with strong character, than the rest of promoters (with valences of 2 to 3, except to Mo), giving rise to a greater quantitative acidity of this catalyst. Molybdenum exhibits a lower reducibility, which resulted in a lower incorporation of acid centres, and therefore

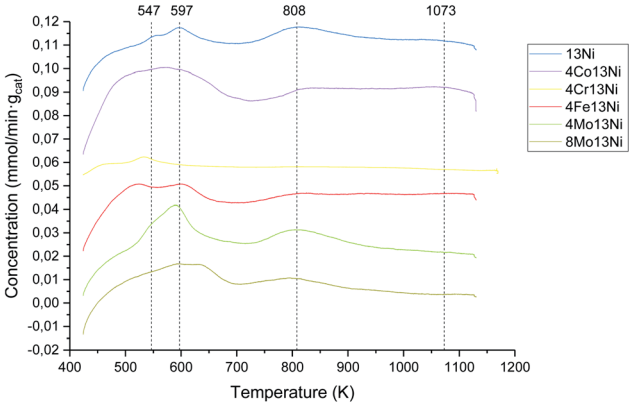

Fig. 4 NH_3-TPD profiles of the prepared catalysts in 4% H_2/Ar atmosphere and 10 K min^{-1} heating rate.

a lower total acidity. The increase in acidity in the remaining bimetallic catalysts may be due to the incorporation of metal atoms in the support structure.[50]

The CO_2-TPD profiles are shown in Fig. S2,† while the amount and strength of basic centres, related to μmoles of CO_2 desorbed per gram of catalyst, are shown in Table 2. According to the force of interaction of CO_2 with the basic centres of the catalyst, determined by the temperature that is necessary to release the CO_2, three regions are identified. Weak basic centres between 313 K and 423 K, moderate basic centres between 423 and 723 K and strong basic centres between 723 and 873 K. It is possible to identify three peaks in the TPD profiles, corresponding on the one hand with weak bonds corresponding to bicarbonate species formed by the CO_2 molecules on the surface of the catalyst in the low temperature region. On the other hand, at higher temperatures, in the temperature region corresponding to moderate interaction with the basic centres, the peak found is associated with bicarbonate species and bicarbonate monodentate species give rise to the peak observed at higher temperatures (associated with strong interactions).[51] All the catalysts analysed have a similar interaction with CO_2 being the commercial catalyst the most basic one. It is also remarkable that the number of strong basic centres. This demonstrates the strong character of the interactions of these catalysts with CO_2, interacting with the monodentate species of the bicarbonate species.

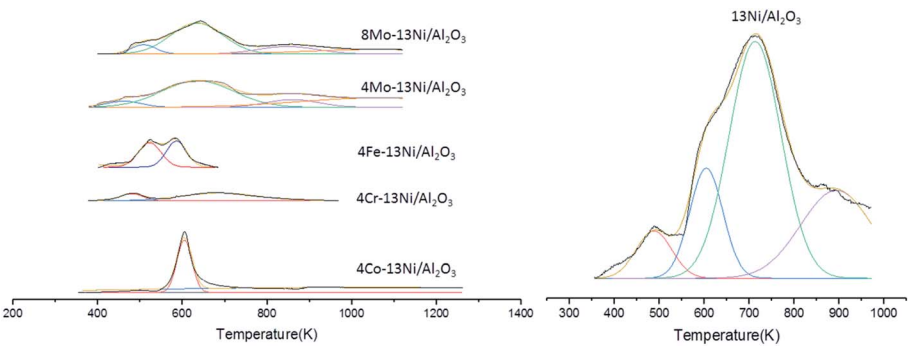

Fig. 3 Gaussian fitted curves of H_2-TPR patterns for the prepared catalysts.

Table 2 Distribution of the strength of acidity by NH_3-TPD and basicity by CO_2-TPD of the catalysts

	Acidity (μmol NH_3 per g_{cat})			Basicity (μmol CO_2 per g_{cat})		
Catalyst	Weak	Medium	Strong	Weak	Medium	Strong
Temperature (K)	<523	523 < T < 673	>673	<423	423 < T < 723	>723
Commercial				12.64	61.19	115.64
13Ni/Al_2O_3	145.89	346.79	1118.73	10.95	56.97	100.82
4Co–13Ni/Al_2O_3	244.20	512.97	1338.98	8.17	54.26	108.78
4Cr–13Ni/Al_2O_3	237.11	732.28	1809.12	11.56	60.78	110.05
4Fe–13Ni/Al_2O_3	192.20	389.72	1172.34	8.60	55.64	106.59
4Mo–13Ni/Al_2O_3	149.83	454.23	1097.76	8.67	52.80	94.72
8Mo–13Ni/Al_2O_3	176.83	420.23	987.5	9.45	52.28	95.74

3.1.5 SEM, TEM and STEM. The morphology of the different catalysts was studied employing the techniques SEM, TEM and STEM. These micrographs show few morphological differences between fresh and deactivated, after reaction, catalysts. Applying EDX analysis to metal and sulphur atoms, presence of sulphur in the used catalysts after regeneration was detected, being remarkable in the 4Cr–13Ni/alumina catalyst. Pictures showing the results are shown in ESI as Fig. S3–S9.†

Regarding the SEM pictures, they do not allow any meaningful conclusion. As the atomic weight of the metal atoms involved are quite close, it is difficult to distinguish if there are interaction between Ni and promoter.[52] Thus, STEM-EDX images of used catalysts were analysed. They suggest that only in the catalysts containing cobalt (Fig. S4†)[53] and molybdenum as second metal (Fig. S7 and S8†) there is a significant interaction between the promoter metal and nickel species, which could indicate that they really are bimetallic catalysts. However, in iron (Fig. S6†) or chromium (Fig. S5†) catalysts, Ni with little interaction with promoters is observed. The promoter metals are located in the pore structure of the catalyst along with the Ni species.

In the catalysts 13Ni/Al_2O_3 and 4Co–13Ni/Al_2O_3 (Fig. S3 and S4†) a high dispersion of the metallic centres was observed throughout the surface of the porous support. The dispersion was calculated with eqn (9) from the nickel particle size values determined from the measurements made in STEM. The metal particles present in these catalysts have an average size value between 4.41 and 10.03 nm, as summarized in Table 3, as a result of the size measurement of more than 200 metal particles in each case. On the contrary, catalysts 4Cr–13Ni/Al_2O_3, 4Fe–13Ni/Al_2O_3, 4Mo–13Ni/Al_2O_3 and 8Mo–13Ni/Al_2O_3 (Fig. S5–S8†) exhibit a larger size of metal particles, between approximately 5.33 and 16.5 nm, due in part to the accumulation of these atoms in the form of agglomerates. This resulted in a smaller dispersion of the metallic atoms onto the alumina surface, as it was checked by EDX.

In addition, as explained below by the XRD, the metal crystal size is close in all cases to 5 nm. This implies that from a morphological point of view, in those cases in which a larger particle size is determined, the sintering of several of these crystals. This phenomenon is remarkable in the case of nickel, where a higher metal content results in a greater extent of accumulation of these atoms, giving rise to metallic agglomerates. This may involve a decrease in the activity of the catalyst.

Regarding the formation of metal sulphides, in Fig. S9† a significant amount of sulphur in all catalysts is detected. Even taking into account that a regeneration procedure with oxygen was applied.

3.1.6 XPS. The surface species of the catalyst were analysed by XPS, identifying the main metals and their oxidation states. The catalysts studied, based on Ni, showed three peaks at 852.9, 857 and 862.3 eV according to Ni^0, Ni^{2+} from $NiAl_2O_4$, and Ni^{2+}

Table 3 Average metal particle size and Ni dispersion of the catalysts determined by STEM measurements

	Particle size (nm)		
	Ni	Promoter metal	Ni dispersion
13Ni/Al_2O_3	10.03	—	0.10
4Co–13Ni/Al_2O_3	4.41	8.36	0.23
4Cr–13Ni/Al_2O_3	6.72	5.33	0.15
4Fe–13Ni/Al_2O_3	11.12	7.59	0.09
4Mo–13Ni/Al_2O_3	12.31	10.20	0.08
8Mo–13Ni/Al_2O_3	16.50	8.47	0.06

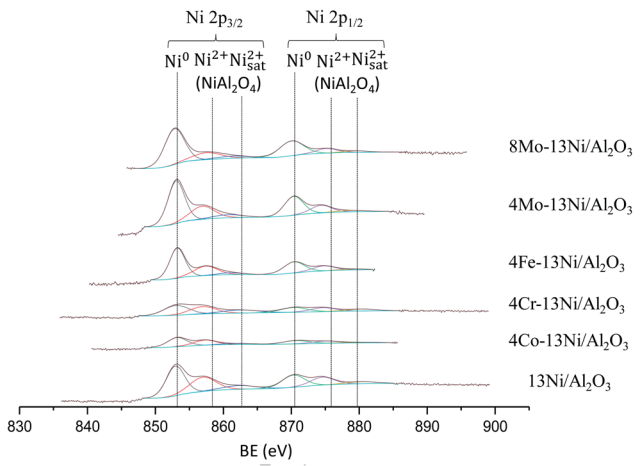

Fig. 5 XPS spectra of Ni $2p_{3/2}$ and $2p_{1/2}$ regions of fresh mono- and bimetallic catalysts.

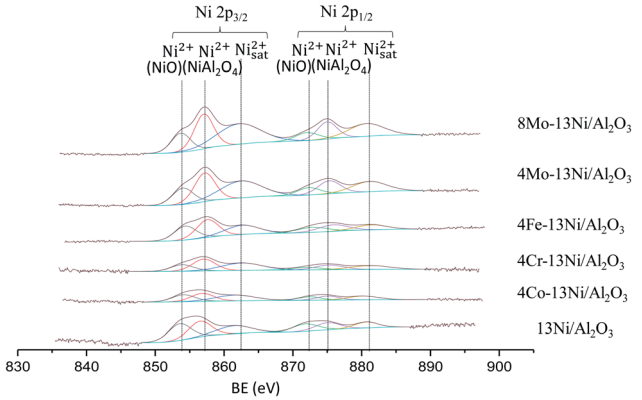

Fig. 6 XPS spectra of Ni $2p_{3/2}$ and $2p_{1/2}$ regions of used mono- and bimetallic catalysts.

satellite respectively for fresh catalyst,[54] as observed in Fig. 5. Used catalyst showed also three peaks, at 854, 857 and 862.3 eV, corresponding to Ni^{2+} from NiO, Ni^{2+} from $NiAl_2O_4$, and Ni^{2+} satellite respectively, as observed in Fig. 6. It is observed that the Ni forming the $NiAl_2O_4$ is not reducible. Its value does not change in the monometallic catalyst after its use in the reaction. In bimetallic catalysts a significant increase in nickel aluminate is observed due to the effect of the temperature and the sintering of the catalyst. This transformation causes the disappearance of metallic nickel, which produces the oxidation of the remaining Ni, as observed in Table 4. This justifies the loss of activity that takes place in the catalysts after their use in the reaction, especially at high temperatures and after the use of a stream of gases containing H_2S.

The presence of the secondary metal was detected by XPS, however it was not possible to quantify it due to the superposition with the Auger LMM line of Ni in the case of the catalyst $4Co–13Ni/Al_2O_3$ and $4Fe–13Ni/Al_2O_3$. However, chromium and molybdenum could be analysed by this technique, appearing in the positions 577.7 and 586.3 eV for the Cr oxides 2p (3/2 and 1/2 respectively); 228.1 and 231.1 eV for the metallic Mo ($3d_{5/2}$) and 232 and 235 eV for the MoO_3 ($3d_{5/2}$). It is observed that the amount of quantified Cr does not vary after its use in the reaction (from 1.3% to 1.4%). However, in the case of Mo, the amount of oxide does not vary after the use of the catalyst, but the amount of Mo metal does, which is considerably reduced (from 8.8% to 1.7% for 8Mo and from 1% to 0.34% for 4Mo).

Table 4 Concentration percentage of metallic Ni^0, Ni^{2+} from NiO and Ni^{2+} from $NiAl_2O_4$, with respect to the total

	Fresh catalyst		Used catalyst	
	Ni^0	Ni^{2+} ($NiAl_2O_4$)	Ni^{2+} (NiO)	Ni^{2+} ($NiAl_2O_4$)
$13Ni/Al_2O_3$	0.94	0.63	0.65	0.61
$4Co–13Ni/Al_2O_3$	0.34	0.22	0.27	0.31
$4Cr–13Ni/Al_2O_3$	0.44	0.34	0.92	0.46
$4Fe–13Ni/Al_2O_3$	0.63	0.30	0.46	0.58
$4Mo–13Ni/Al_2O_3$	1.09	0.48	0.53	0.93
$8Mo–13Ni/Al_2O_3$	1.90	0.52	0.74	1.34

Table 5 Metal/Al ratio obtained by XPS analysis of the different catalysts studied (M = Cr or Mo)

	Fresh catalyst		Used catalyst	
	M/Al	Ni/Al	M/Al	Ni/Al
$13Ni/Al_2O_3$		0.067		0.069
$4Co–13Ni/Al_2O_3$		0.023		0.040
$4Cr–13Ni/Al_2O_3$	0.033	0.038	0.040	0.054
$4Fe–13Ni/Al_2O_3$		0.038		0.059
$4Mo–13Ni/Al_2O_3$	0.048	0.069	0.035	0.112
$8Mo–13Ni/Al_2O_3$	0.363	0.127	0.126	0.203

This reduction is due to sintering of the metal, which produces an agglomeration in deeper layers of the catalyst.

The analyses have detected the presence of carbon in the catalysts, due to the formation and deposition in the reaction process. The proportions of metal to aluminium in the catalysts analysed was collected in Table 5, for the results obtained in the XPS analyses. The incorporation of the promoter reduces the proportion of Ni/Al considerably in all catalysts, with the exception of catalysts with Mo, in which it increases, with molybdenum being part of the catalyst bulk coordinating with the Ni on the surface. The use of the catalyst in the reaction reduces the ratio of the secondary metal to Al, increasing that of Ni/Al, especially in the catalysts promoted by Mo. This justifies that the wear of the catalyst with the high temperature and the poisoning with H_2S not only produces the oxidation of the Ni, but it also the NiS formation, during the reaction, that could increase the sintering of the catalyst.[55] After removing the H_2S stream and the corresponding regeneration step, the sulphur containing compounds in the catalyst are removed, not being detected in the XPS analyses. However, it does result in loss of activity and the disability to recover activity.

3.1.7 XRD. The X-ray diffraction (XRD) is an analysis used for phase identification of a crystalline material of the catalyst and the determination of the dimensions of crystal size. The XRD patterns of the bimetallic and monometallic fresh-reduced catalysts supported over Al_2O_3, are shown in Fig. 7. This figure report the pattern from 20° to 90°, being located the highest peaks between 30° and 70°. The XRD pattern of the $13Ni/Al_2O_3$

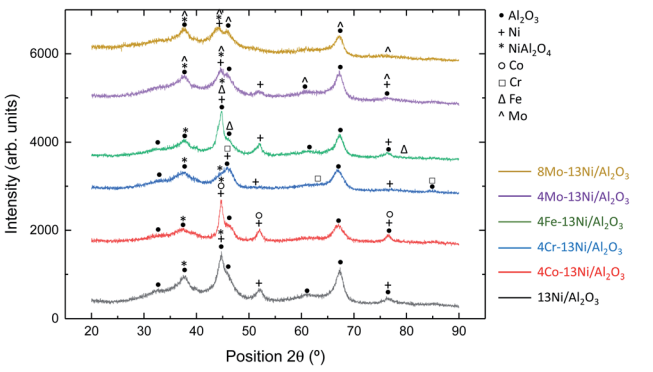

Fig. 7 XRD patterns of bi- and monometallic fresh-reduced catalysts supported over Al_2O_3.

showed the characteristics peaks of Ni metallic and Al_2O_3 support. In comparison with the XRD patterns of the other catalysts, the significant peaks measured in all the cases coincided in Ni peaks (44.8° and 52°) and Al_2O_3 peaks (32.2°, 37.7°, 39.5°, 46.4° and 67.3°). According to these analyses, the Al_2O_3 support and metallic Ni were the main phases detected. The low crystallinity of the samples and the overlap of nickel peak with the second metallic species, as shown in Table 6, make difficult a clear identification of the phases present in each sample.

The analysis of the XRD pattern revealed the effect of adding a second metal, widening the Ni and Al_2O_3 characteristic peaks, reducing the intensity of the signal and moving slightly the 2θ position of these peaks. The XRD pattern of the catalysts used, presented in the Fig. 8 showed, in general, a lower amount of elements in a reduced state, as observed specially in the 4Co–13Ni/Al_2O_3 spectrum, due to the sintering process at high temperature and the presence of H_2S.

The 2θ position of the crystalline phases determined from Joint Committee on Powder Diffraction Standards (JCPDS) database, are represented on the Fig. 7 and 8 for the different species of the catalysts. These results are collected in the Table 6, contrasted with the bibliography.[56–59]

The crystallite size was determined from XRD technique by applying the Scherrer equation, and collected in Table 1. The crystallite sizes were calculated using the most representative XRD peak that does not overlap those of other crystals. Values around 5 nm for all the catalysts analysed were obtained, and in contrast with higher values measured by TEM, SEM and STEM for the nickel particles. The XRD analysis showed the low value of crystallinity of the samples. For the Co sample, $NiCo_2O_4$ was formed due to the interaction between Ni and Co.[45] For the Fe sample, XRD corroborated that NiFe alloy was not formed and only small amounts of Fe_2O_3. The main peaks mentioned in Table 6 for the Mo revealed the presence of MoO_3 but no separated signals were detected for metal nickel and MoO_3.[60]

3.2. Activity tests

Nickel is a metal commonly used in CO_2 methanation for the high yields to methane achieved.[61] Therefore, the catalysts employed in this work, are based on nickel as active metal, supported on alumina due to high surface area. In order to improve the catalytic activity and H_2S resistance of the nickel–alumina system (13Ni/Al_2O_3), a second metal was added modifying the physical and chemical properties. The metals

Table 6 XRD crystalline phases for the catalysts

Phase	JCPDS code	Value (°)
Ni fcc structure	087-0712	44.5, 51.6, 76.7
Al_2O_3	077-0396	32.2, 37.7, 39.5, 46.4, 67.3
$NiAl_2O_4$	073-0239	37.2, 44.2, 64.3
Metallic β-Co	015-0806	44.7, 52, 76.6
Cr	001-1250	43.8, 64, 82
Fe	088-2324	44.8, 46, 79
Mo	088-2331	37.6, 44.2, 45.8, 65, 79, 83.8

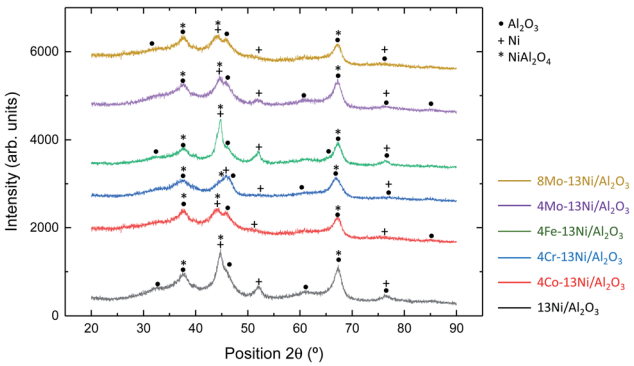

Fig. 8 XRD patterns of bi- and monometallic used-reduced catalysts supported over Al_2O_3.

employed are transition metals in a quantity of 4 wt% in all the cases (4Cr–13Ni/Al_2O_3, 4Co–13Ni/Al_2O_3, 4Fe–13Ni/Al_2O_3 and 4Mo–13Ni/Al_2O_3) and 8 wt% (8Mo–13Ni/Al_2O_3) also in the case of the molybdenum, as was indicated and justified in the introduction.

The activity was measured as CH_4 yield obtained at each temperature analysed for the different mono and bimetallic nickel–alumina catalysts. The results obtained for the activity tests are shown in Fig. 9 (zoom of the graphic between 220–500 K has been included in ESI, Fig. S10†).

In the tests without presence of H_2S, 4Mo–13Ni/Al_2O_3, 8Mo–13Ni/Al_2O_3, 4Fe–13Ni/Al_2O_3 and 4Co–13Ni/Al_2O_3 presented lower yields at low temperatures than the monometallic. It was necessary to increase the reaction temperature above 623 K to reach the highest yields. At 723 K, the catalysts reached the maximum methane yields in the temperature range studied, reaching in all cases a maximum value close to the thermodynamic equilibrium, except for the 8Mo–13Ni/Al_2O_3 catalyst that did not reached this maximum at the temperatures studied. Once the temperature of this maximum has been exceeded, the yield falls parallel to the trend of thermodynamic equilibrium, with the methane yield remaining in all cases around 80% for the maximum temperatures analysed, except for molybdenum catalysts. The iron catalyst exhibits the highest yield values together with the commercial catalyst. Subsequently, the

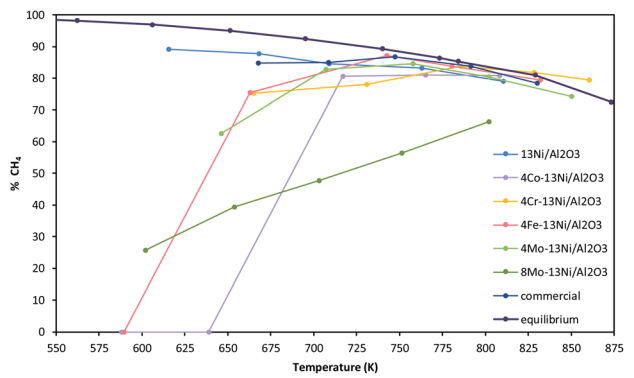

Fig. 9 Methane yield obtained for the catalysts supported on alumina.

trajectory of the methane yield curve of these catalysts, as the temperature increases, is similar in the range studied.

According to Rönsch's *et al.* work,[62] the activity should be greater for Fe than for Ni, followed by Co and finally by Mo. In the case of selectivity, it is mentioned that the monometallic Ni catalyst is the one with the highest yield to methane, followed by the bimetallic with Co and finally with Fe. In the case of Frontera *et al.*[63] according to the calculated activity from volcano curve and economic considerations, the catalysts with Ni–Fe alloys can be considered good candidates for CO_2 methanation. Thus, this is accordance with the highest yield achieved for the Fe bimetallic catalyst. For the Mo bimetallic catalyst, the one with the lower activity, it appeared with the lower theoretical activity, but it was used in order to improve the sulphur resistance.

The methanation tests continued in the presence of H_2S until catalyst deactivation Fig. 10. The addition of 50 ppm of H_2S to the reaction feed rapidly reduced the activity of 4Co–13Ni/Al_2O_3 and 4Fe–13Ni/Al_2O_3 catalysts, until their complete deactivation in approximately 50 min. The catalysts 4Cr–13Ni/Al_2O_3, 4Mo–13Ni/Al_2O_3 and the monometallic (13Ni/Al_2O_3) showed a higher resistance, than the previous ones, to the action of H_2S, being completely deactivated after 80 min. The greatest resistance to the inhibitory action of H_2S among the prepared catalysts was the 8Mo–13Ni/Al_2O_3 catalyst, which was not deactivated until 100 min. However, the most stable catalyst in the presence of H_2S is the commercial catalyst, which maintains its catalytic activity until 120 min, before starting its deactivation, which was completed at 170 min.

After deactivation of the catalysts in the presence of H_2S, the auto-regeneration capacity of the catalysts was studied eliminating this gas from the feed at 500 °C. In all the cases analysed, the catalysts did not recover the activity.

Finally, the catalysts were regenerated, employing a mixture of 3% O_2 in N_2, in order to eliminate the NiS species and carbon depositions (increased by Ni–S presence), blocking the catalyst's active centres.[55] Afterwards, the catalysts were reactivated reducing with H_2. The recovered catalyst was used in a reaction stage, at 500 °C. It was observed that the catalysts activity as methane yield was not recovered, with the exception of the 4Co–13Ni/Al_2O_3 catalyst, that recovers a methane yield of about 13%. During the reaction, deactivation, and after regeneration stage, the presence of CO was not detected as it can be produced as a by-product due to the reverse water gas shift reaction.

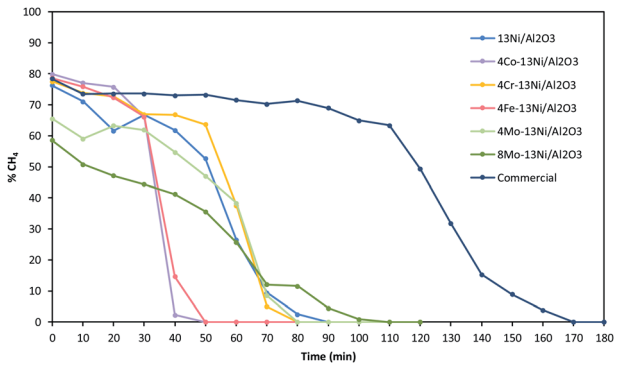

Fig. 10 Catalysts deactivation due to 50 ppm of H_2S at 773 K.

3.3. Discussion

Nickel has proved to be the catalyst with the best characteristics in the methanation reaction, reaching a high yield (89.05%) to methane at low temperatures (615.2 K), in accordance with the work of Muroyama *et al.*[22] for a 10Ni/Al_2O_3 catalyst calcined at 873 K.

However, the work of García *et al.*[13] and Garbarino *et al.*,[21] done at temperatures around 673 K, obtained methane yields significantly lower (approximately 50%). This shows that the temperature has great influence on the start of the reaction, so that there is an interval, characteristic for each catalyst, below which the reaction does not occur (or with low performance), with a higher temperature being necessary to overcome the activation energy of that system. This fact was observed by comparison with other catalysts, such as 4Co–13Ni/Al_2O_3 or 4Fe–13Ni/Al_2O_3. The addition of a suitable metal promoter produces the modification of reaction ignition temperature of the nickel catalyst.

The high performance of this monometallic catalyst can be justified by its particular characteristics observed in the characterization: the high specific area, determined by BET, indicates a high dispersion of the metallic sites, which are reduced at operating temperature as demonstrated in the H_2-TPR profiles. The metallic centres were observed by SEM and TEM, which present a small size, without the formation of agglomerates and well distributed over the entire surface. The nickel, as indicated by the XPS and XRD analysis, is mainly reduced and/or $NiAl_2O_4$.

This catalyst has similarities with the 4Co–13Ni/Al_2O_3, sharing the characteristic of being composed of metallic centres of small size with high dispersion, as can be deduced from the analysis of SEM and TEM. These active centres are dispersed on the surface of the catalyst, which has a larger surface area than the rest of the catalysts (as analysed in BET). This coincides with that observed by Wang *et al.*[64] for Co and Mo catalysts. In this work, the use of these catalysts is also justified by the inhibition in the formation of S^{2-}. This may justify the greater resistance that the catalysts of Mo have to the deactivation with H_2S and the capacity of recovery of the catalytic activity of the Co catalyst, recovering the yield up to 13%. The performance values of the Co catalyst are consistent with what Alrafei *et al.*[65] demonstrated in his work, where they studied how the proportion of Co and Ni affects the reaction of CO_2 methanation. According to this work, Co is an active metal in this reaction. However, the lower activity in methanation of this metal indicates the blocking of some active centres, as observed in the reduction of the metal/Al ratio in the 4Co–13Ni/Al_2O_3 catalyst with respect to 13Ni/Al_2O_3.

The addition of Mo improves the resistance of the Ni catalyst to H_2S, as justified above. However, the added amount of this promoter affects the catalytic capacity of Ni, so that as the Mo ratio increases (from 4 to 8), the greater the resistance to H_2S but the catalyst yield is lower. This phenomenon was reported Maluf's *et al.*[66] work, where they used a Ni : Al molar ratio of 3,

with different proportions of Mo (0.05, 05, 1.0 and 2.0 wt%) as a promoter and Ni (60 wt%) for steam reforming. They observed that using the optimal amount of Mo as a promoter, improves the yield, avoiding the formation of CO. This effect occurs due to the blocking of the active centres of the Ni by the Mo, verified by the reduction of the specific surface in BET and the greater presence of this metal than the Ni in the analysis in XPS. At low amounts of Mo, the activity improves as a result of the transfer of electrons from the MoO_x of the surface to Ni, increasing the electronic density of the metallic Ni.[66]

The 4Fe–13Ni/Al_2O_3 catalyst needs to reach a temperature of 663 K for the methanation reaction to take place, needing a lower temperature than the 4Co–13Ni/Al_2O_3 catalyst. This is in contrast to Lu's *et al.*[26] work, where Co addition on ZrO_2 modified mesoporous clays had a similar contribution to Fe on CO_2 conversion. Although it explains the similarity in methane yield of both catalysts at higher temperatures. Furthermore, in the SEM analysis, a similar morphology was observed between the Co and Fe catalyst, although there is a lower dispersion of the metal centres when agglomerates appear in fibrous structures, which are distinguished in TEM.

The low specific surface area and the smaller micropore surface determined in BET justify a greater exposure of the active centres. It is verified by observing the metal/Al ratio of the XPS analysis and the metal distribution in SEM. Due to the arrangement of these metal centres (in a similar way to the iron catalyst) with homogeneously dispersed agglomerated particles, they are more accessible. Therefore, the reaction is initiated with high methane yield. This is also why the amount of Cr that is added to the system has a great influence, as demonstrated by Liu *et al.*[67] for the CO methanation with OMA as support, with a 10 wt% of Ni and different proportion of Cr as promoter. So that, the adequate amount of promoter has a positive effect on the catalyst, while high amounts can block the active centres of the other metal (Ni in this case) and low amounts do not bring any benefit to the system. In this case, the amount used is among the most favourable values for the methanation reaction, according to this work.

Finally, other interesting method used to measure the catalyst activity is the turnover frequency (TOF). In this work turnover frequency of CO_2 (h^{-1}) is employed to compare the quality of available active centres, based on the Ni particles sizes and their dispersion, with respect to the total amount of Ni atoms. TOF values obtained for the catalysts analysed are shown in Table 1. As expected, catalysts with smaller particle size have a higher dispersion, as in the 4Co–13Ni/Al_2O_3 and 4Cr–13Ni/Al_2O_3 catalysts (Table 3). Similar results were reported by Aziz *et al.*,[68] showing that a balance between the Ni dispersion and basic site concentration led to the optimum CO_2 conversion over the 5 wt% Ni/SiO_2 catalyst. In the present work, this comparison is more complicated due to the fact that catalyst included a second promoter.

As an example, the catalysts 4Mo–13Ni/Al_2O_3, 8Mo–13Ni/Al_2O_3, and 4Fe–13Ni/Al_2O_3, follow the general rule of a higher dispersion (Table 4) results and a higher CO_2 conversion and, in this case, a higher value of TOF. However, when compared this catalysts with 4Fe–13Ni/Al_2O_3, the tendency is different, this catalyst presented the highest dispersion, but a low activity, and then a low TOF. One possible explanation of this effect is the interaction of Ni with the promoter. As it can be seen comparing Fig. S3–S6,† the catalyst presenting the highest interaction between Ni and promoter (yellow areas) is the 4Co–13Ni/Al_2O_3, and this is the catalyst with the highest dispersion (lowest Ni particle size) and the lowest activity. This result is in agreement with the conclusion presented by Italiano *et al.*[51] They stated that CO_2 hydrogenation was affected by the nature of active centres rather than the number of active sites available to perform methanation reaction. In this case, this close interaction hinders the Ni activity. Nevertheless, also this close interaction has a beneficial effect when sulphur is present in the reaction media, as the 4Co–13Ni/Al_2O_3 is the catalyst that revealed the best deactivation tolerance.

Regarding the relationship between TOF and basicity, there is not a clear correlation. In this case, it seems that the interaction with the metallic active centers is the most important parameter.

Finally, the regeneration procedure employed to recover initial activity of the catalysts was not successful as sulphur was detected by STEM. This seems to be responsible for the loss of catalytic activity. In ESI, Fig. S9,† for the 4Co–13Ni/Al_2O_3 catalyst, it can be observed the presence of S interacting with both the active metal and the promoter.

4. Conclusions

The CO_2 methanation was studied over a 13Ni/Al_2O_3, and 4Co–13Ni/Al_2O_3, 4Cr–13Ni/Al_2O_3, 4Fe–13Ni/Al_2O_3, 4Mo–13Ni/Al_2O_3 and 8Mo–13Ni/Al_2O_3 modified catalysts. The promoter was integrated in the catalyst attached to the Ni metal centres, reducing the dispersion and forming agglomerates, with the exception of the catalyst of 4Co–13Ni/Al_2O_3, as observed by SEM and EDX, and as it was verified by XPS. The catalytic activity of the Ni modified catalysts is improved being positive between 700 and 800 K for all the catalysts except for 8Mo–13Ni/Al_2O_3. Mo in small quantities improves the methanation reaction, but at high concentration levels it blocks the Ni active centres, reducing the activity of the catalyst. The best catalytic system to operate above 700 K was the promoted by iron, reaching the highest methane yield (87%) at 742 K.

The second objective of adding a promoter to the Ni catalyst was the improvement of its resistance to H_2S poisoning, achieved in the 8Mo–13Ni/Al_2O_3 catalyst. The resistance to 50 ppm of H_2S in the reaction gases was increased from 90 to 120 min. The addition of Cr increased the stability of the catalytic activity before starting to deactivate from 10 to 60 min.

Finally, the third objective of the use of promoters consisted in the improvement of the recovery capacity of the catalyst to the deactivation by poisoning with H_2S. The only catalyst able to recover the catalytic activity up to a 13% of CH_4 yield, after a stage of regeneration and reactivation, was the 4Co–13Ni/Al_2O_3 catalyst, by inhibiting the formation of the S^{2-} bond on the metal surface.

Upgrading promoters to nickel catalyst has benefited the performance of the catalyst system in several ways, depending

on the metal used. Improving performance is related to an increase in metal dispersion in some cases, an improvement in the interaction between metals that can reduce the effect of temperature compared to deactivation by sintering in other cases, or finally an improvement in resistance to H_2S poisoning. In future works, a larger study of the metal charge would be interesting to improve its positive effect on the catalyst, with different catalyst concentrations that allow a better comparison between the study catalyst systems.

Conflicts of interest

There are no conflicts to declare.

Acknowledgements

This research was supported by the University of the Basque Country (UPV/EHU), Basque Government (IT993-16), Spanish Ministry of Economy and Competitiveness (ENE2017-82250-R) and European Union through the European Regional Development Fund (FEDER). The authors thank for technical and human support provided by SGIker of UPV/EHU and European Funding (ERDF and ESF).

References

1 A. Antenucci and G. Sansavini, Extensive CO_2 recycling in power systems *via* power-to-gas and network storage, *Renewable Sustainable Energy Rev.*, 2019, **100**, 33–43, DOI: 10.1016/j.rser.2018.10.020.

2 J. Pollex and A. Lenschow, Surrendering to growth? The European Union's goals for research and technology in the Horizon 2020 framework, *J. Cleaner Prod.*, 2018, **197**(2), 1863–1871.

3 A. Lewandowska-Bernat and U. Desideri, Opportunities of power-to-gas technology, *Energy Procedia*, 2017, **105**, 4569–4574, DOI: 10.1016/j.egypro.2017.03.982.

4 A. Berrada and K. Loudiyi, Operation, sizing, and economic evaluation of storage for solar and wind power plants, *Renewable Sustainable Energy Rev.*, 2016, **59**, 1117–1129, DOI: 10.1016/j.rser.2016.01.048.

5 J. Kotowicz, D. Węcel and M. Jurczyk, Analysis of component operation in power-to-gas-to-power installations, *Appl. Energy*, 2018, **216**, 45–59, DOI: 10.1016/j.apenergy.2018.02.050.

6 H. Chen, T. N. Cong, W. Yang, C. Tan, Y. Li and Y. Ding, Progress in electrical energy storage system: a critical review, *Prog. Nat. Sci.*, 2009, **19**, 291–312, DOI: 10.1016/j.pnsc.2008.07.014.

7 P. Colbertaldo, G. Guandalini and S. Campanari, Modelling the integrated power and transport energy system: the role of power-to-gas and hydrogen in long-term scenarios for Italy, *Energy*, 2018, **154**, 542–601.

8 J. Chi and H. Yu, Water electrolysis based on renewable energy for hydrogen production, *Chin. J. Catal.*, 2018, **39**, 390–394, DOI: 10.1016/S1872-2067(17)62949-8.

9 I. A. Gondal, Hydrogen integration in power-to-gas networks, *Int. J. Hydrogen Energy*, 2019, **44**, 1803–1815, DOI: 10.1016/j.ijhydene.2018.11.164.

10 S. Tada, S. Ikeda, N. Shimoda, T. Honma, M. Takahashi, A. Nariyuki and S. Satokawa, Sponge Ni catalyst with high activity in CO_2 methanation, *Int. J. Hydrogen Energy*, 2017, **42**(51), 30126–30134.

11 S. Appari, V. M. Janardhanan, R. Bauri and S. Jayanti, Deactivation and regeneration of Ni catalyst during steam reforming of model biogas: an experimental investigation, *Int. J. Hydrogen Energy*, 2014, **39**, 297–304, DOI: 10.1016/j.ijhydene.2013.10.056.

12 R. Chein and Z.-W. Yang, H_2S effect on dry reforming of biogas for syngas production, *Int. J. Energy Res.*, 2019, **43**, 3330–3345, DOI: 10.1002/er.4470.

13 I. García-García, U. Izquierdo, V. L. Barrio, P. L. Arias and J. F. Cambra, Power-to-gas: storing surplus electrical energy. Study of Al_2O_3 support modification, *Int. J. Hydrogen Energy*, 2016, **41**, 19587–19594, DOI: 10.1016/j.ijhydene.2016.04.010.

14 D. H. Moon, W. J. Chung, S. W. Chang, S. M. Lee, S. S. Kim, J. H. Jeung, Y. H. Ro, J. Y. Ahn, W. Guo, H. H. Ngo and D. D. Nguyen, Fabrication and characterization of Ni-Ce-Zr ternary disk-shaped catalyst and its application for low-temperature CO_2 methanation, *Fuel*, 2020, **260**, 116260, DOI: 10.1016/j.fuel.2019.116260.

15 J. Y. Ahn, S. W. Chang, S. M. Lee, S. S. Kim, W. J. Chung, J. C. Lee, Y. J. Cho, K. S. Shin, D. H. Moon and D. D. Nguyen, Developing Ni-based honeycomb-type catalysts using different binary oxide-supported species for synergistically enhanced CO_2 methanation activity, *Fuel*, 2019, **250**, 277–284, DOI: 10.1016/j.fuel.2019.03.123.

16 Z. Zhang, T. Wei, G. Chen, C. Li, D. Dong, W. Wu, Q. Liu and X. Hu, Understanding correlation of the interaction between nickel and alumina with the catalytic behaviors in steam reforming and methanation, *Fuel*, 2019, **250**, 176–193, DOI: 10.1016/j.fuel.2019.04.005.

17 L. Falbo, C. G. Visconti, L. Lietti and J. Szanyi, The effect of CO on CO_2 methanation over Ru/Al_2O_3 catalysts: a combined steady-state reactivity and transient DRIFT spectroscopy study, *Appl. Catal., B*, 2019, **256**, 117791, DOI: 10.1016/j.apcatb.2019.117791.

18 A. Alarcón, J. Guilera, R. Soto and T. Andreu, Higher tolerance to sulfur poisoning in CO_2 methanation by the presence of CeO_2, *Appl. Catal., B*, 2020, **263**, 118346, DOI: 10.1016/j.apcatb.2019.118346.

19 M. Trueba and S. P. Trasatti, γ-Alumina as a support for catalysts: a review of fundamental aspects, *Eur. J. Inorg. Chem.*, 2005, 3393–3403, DOI: 10.1002/ejic.200500348.

20 G. Garbarino, D. Bellotti, P. Riani, L. Magistri and G. Busca, Methanation of carbon dioxide on Ru/Al_2O_3 and Ni/Al_2O_3 catalysts at atmospheric pressure: catalysts activation, behaviour and stability, *Int. J. Hydrogen Energy*, 2015, **40**, 9171–9182, DOI: 10.1016/j.ijhydene.2015.05.059.

21 G. Garbarino, P. Riani, L. Magistri and G. Busca, A study of the methanation of carbon dioxide on Ni/Al_2O_3 catalysts at

atmospheric pressure, *Int. J. Hydrogen Energy*, 2014, **39**, 11557–11565, DOI: 10.1016/j.ijhydene.2014.05.111.

22 H. Muroyama, Y. Tsuda, T. Asakoshi, H. Masitah, T. Okanishi, T. Matsui and K. Eguchi, Carbon dioxide methanation over Ni catalysts supported on various metal oxides, *J. Catal.*, 2016, **343**, 178–184, DOI: 10.1016/j.jcat.2016.07.018.

23 Z. Li, K. Zhang, W. Wang, J. Qu, Y. Tian, B. Wang and X. Ma, Kinetics of sulfur-resistant methanation over supported molybdenum-based catalyst, *J. Taiwan Inst. Chem. Eng.*, 2016, **68**, 239–245, DOI: 10.1016/j.jtice.2016.08.043.

24 M. J. Kim, S. H. Park and D. B. Lee, Corrosion of Fe-2.25% Cr-1% Mo steels at 600–800 °C in $N_2/H_2O/H_2S$ atmospheres, *Energy Procedia*, 2012, **14**, 1837–1842, DOI: 10.1016/j.egypro.2011.12.1176.

25 G. Wang, S. Xu, L. Jiang and C. Wang, Nickel supported on iron-bearing olivine for CO_2 methanation, *Int. J. Hydrogen Energy*, 2016, **41**, 12910–12919, DOI: 10.1016/j.ijhydene.2016.06.066.

26 H. Lu, X. Yang, G. Gao, J. Wang, C. Han, X. Liang, C. Li, Y. Li, W. Zhang and X. Chen, Metal (Fe, Co, Ce or La) doped nickel catalyst supported on ZrO_2 modified mesoporous clays for CO and CO_2 methanation, *Fuel*, 2016, **183**, 335–344, DOI: 10.1016/j.fuel.2016.06.084.

27 L. Pastor-Pérez, V. Patel, E. Le Saché and T. R. Reina, CO_2 methanation in the presence of methane: catalysts design and effect of methane concentration in the reaction mixture, *J. Energy Inst.*, 2020, **93**(1), 415–424, https://www.sciencedirect.com/science/article/pii/S1743967118310572.

28 L. Zhang, J.-M. M. Millet and U. S. Ozkan, Deactivation characteristics of Fe–Al–Cu water-gas shift catalysts in the presence of H_2S, *J. Mol. Catal. A: Chem.*, 2009, **309**, 63–70, DOI: 10.1016/j.molcata.2009.04.016.

29 L. Li, C. Howard, D. L. King, M. Gerber, R. Dagle and D. Stevens, Regeneration of Sulfur Deactivated Ni-Based Biomass Syngas Cleaning Catalysts, *Ind. Eng. Chem. Res.*, 2010, **49**, 10144–10148, DOI: 10.1021/ie101032x.

30 Y. Feng, J. Mi, B. Chang, M. Wu, J. Shangguan and H. Fan, Regeneration performance and characteristic of iron oxide/arenaceous sorbents in the atmosphere of O_2/N_2, *Fuel*, 2016, **186**, 838–845, DOI: 10.1016/j.fuel.2016.09.025.

31 B. Wang, Y. Yao, M. Jiang, Z. Li, X. Ma, S. Qin and Q. Sun, Effect of cobalt and its adding sequence on the catalytic performance of MoO_3/Al_2O_3 toward sulfur-resistant methanation, *J. Energy Chem.*, 2014, **23**, 35–42, DOI: 10.1016/S2095-4956(14)60115-7.

32 B.-W. Wang, Y.-Q. Yao, S.-H. Liu, Z.-Y. Hu, Z.-H. Li and X.-B. Ma, Effects of MoO_3 loading and calcination temperature on the catalytic performance of MoO_3/CeO_2 toward sulfur-resistant methanation, *Fuel Process. Technol.*, 2015, **138**, 263–270, DOI: 10.1016/j.fuproc.2015.06.009.

33 Z.-Z. Wang, W.-F. Han and H.-Z. Liu, Hydrothermal synthesis of sulfur-resistant MoS_2 catalyst for methanation reaction, *Catal. Commun.*, 2016, **84**, 120–123, DOI: 10.1016/j.catcom.2016.06.016.

34 M. Wolf, L. H. Wong, C. Schüler and O. Hinrichsen, CO_2 methanation on transition-metal-promoted Ni-Al catalysts: sulfur poisoning and the role of CO_2 adsorption capacity for catalyst activity, *J. CO_2 Util.*, 2020, **36**, 276–287, DOI: 10.1016/j.jcou.2019.10.014.

35 G. V. Franks and L. Meagher, The isoelectric points of sapphire crystals and alpha-alumina powder, *Colloids Surf., A*, 2003, **214**, 99–110, DOI: 10.1016/S0927-7757(02)00366-7.

36 K. M. Hardiman, C.-H. Hsu, T. T. Ying and A. A. Adesina, The influence of impregnating pH on the postnatal and steam reforming characteristics of a Co-Ni/Al_2O_3 catalyst, *J. Mol. Catal. A: Chem.*, 2005, **239**, 41–48, DOI: 10.1016/j.molcata.2005.05.030.

37 T. J. Schildhauer and S. M. A. Biollaz, Synthetic Natural Gas: From Coal, Dry Biomass, and Power-to-Gas Applications, *Focus Catal.*, 2016, **2016**, 7, DOI: 10.1016/j.focat.2016.09.046.

38 C. Cheng, D. Shen, R. Xiao and C. Wu, Methanation of syngas (H_2/CO) over the different Ni-based catalysts, *Fuel*, 2017, **189**, 419–427, DOI: 10.1016/j.fuel.2016.10.122.

39 M. Li, H. Amari and A. C. van Veen, Metal-oxide interaction enhanced CO_2 activation in methanation over ceria supported nickel nanocrystallites, *Appl. Catal., B*, 2018, **239**, 27–35, DOI: 10.1016/j.apcatb.2018.07.074.

40 K. Sing and R. Williams, Physisorption Hysteresis Loops and the Characterization of Nanoporous Materials, *Adsorpt. Sci. Technol.*, 2004, **22**(10), 773–782, DOI: 10.1260/0263617053499032.

41 Y. Bang, S. J. Han, J. G. Seo, M. H. Youn, J. H. Song and I. K. Song, Hydrogen production by steam reforming of liquefied natural gas (LNG) over ordered mesoporous nickel–alumina catalyst, *Int. J. Hydrogen Energy*, 2012, **37**, 17967–17977, DOI: 10.1016/j.ijhydene.2012.09.057.

42 B. Li, Y. Luo, B. Li, X. Yuan and X. Wang, Catalytic performance of iron-promoted nickel-based ordered mesoporous alumina FeNiAl catalysts in dry reforming of methane, *Fuel Process. Technol.*, 2019, **193**, 348–360, DOI: 10.1016/j.fuproc.2019.05.033.

43 D. Raikwar, M. Munagala, S. Majumdar and D. Shee, Hydrodeoxygenation of guaiacol over Mo, W and Ta modified supported nickel catalysts, *Catal. Today*, 2019, **325**, 117–130, DOI: 10.1016/j.cattod.2018.09.039.

44 J. M. Rynkowski, T. Paryjczak and M. Lenik, Characterization of alumina supported nickel-ruthenium systems, *Appl. Catal., A*, 1995, **126**, 257–271, DOI: 10.1016/0926-860X(95)00035-6.

45 S. Valinejad Moghaddam, M. Rezaei, F. Meshkani and R. Daroughegi, Carbon dioxide methanation over Ni-M/Al_2O_3 (M: Fe, CO, Zr, La and Cu) catalysts synthesized using the one-pot sol-gel synthesis method, *Int. J. Hydrogen Energy*, 2018, **43**, 16522–16533, DOI: 10.1016/j.ijhydene.2018.07.013.

46 Z. Fang, D. Shi, N. Lin, A. Li, Q. Wu, Q. Wang, Y. Zhao, C. Feng, Q. Jiao and H. Li, Probing the synergistic effect of Mo on Ni-based catalyst in the hydrogenation of dicyclopentadiene, *Appl. Catal., A*, 2019, **574**, 60–70, DOI: 10.1016/j.apcata.2019.01.026.

47 M. Z. Hossain, M. B. I. Chowdhury and P. A. Charpentier, Effect of surface acidity of Al_2O_3 supported metal catalysts on catalytic activity and carbon deposition during SCWG of

glucose, *Biomass Bioenergy*, 2019, **124**, 142–150, DOI: 10.1016/j.biombioe.2019.04.005.

48 S. A. Yashnik, V. V. Kuznetsov and Z. R. Ismagilov, Effect of χ-alumina addition on H_2S oxidation properties of pure and modified γ-alumina, *Chin. J. Catal.*, 2018, **39**, 258–274, DOI: 10.1016/S1872-2067(18)63016-5.

49 M. Zamani, A. Moradi Delfani and M. Jabbari, Scavenging performance and antioxidant activity of γ-alumina nanoparticles towards DPPH free radical: spectroscopic and DFT-D studies, *Spectrochim. Acta, Part A*, 2018, **201**, 288–299, DOI: 10.1016/j.saa.2018.05.004.

50 S. Ding, Z. Li, F. Li, Z. Wang, J. Li, T. Zhao, H. Lin and C. Chen, Catalytic hydrogenation of stearic acid over reduced NiMo catalysts: Structure–activity relationship and effect of the hydrogen-donor, *Appl. Catal., A*, 2018, **566**, 146–154, DOI: 10.1016/j.apcata.2018.08.028.

51 C. Italiano, J. Llorca, L. Pino, M. Ferraro, V. Antonucci and A. Vita, CO and CO_2 methanation over Ni catalysts supported on CeO_2, Al_2O_3 and Y_2O_3 oxides, *Appl. Catal., B*, 2019, 118494, DOI: 10.1016/j.apcatb.2019.118494.

52 A. Leba and R. Yıldırım, Determining most effective structural form of nickel-cobalt catalysts for dry reforming of methane, *Int. J. Hydrogen Energy*, 2020, **45**, 4268–4283, DOI: 10.1016/j.ijhydene.2019.12.020.

53 J. Horlyck, C. Lawrey, E. C. Lovell, R. Amal and J. Scott, Elucidating the impact of Ni and Co loading on the selectivity of bimetallic NiCo catalysts for dry reforming of methane, *Chem. Eng. J.*, 2018, **352**, 572–580, DOI: 10.1016/j.cej.2018.07.009.

54 *NIST XPS Database, Selected Element Search Result*, https://srdata.nist.gov/xps/EngElmSrchQuery.aspx?EType=PE&CSOpt=Retri_ex_dat&Elm=Ni, accessed July 12, 2019.

55 X. Dou, A. Veksha, W. P. Chan, W.-D. Oh, Y. N. Liang, F. Teoh, D. K. B. Mohamed, A. Giannis, G. Lisak and T.-T. Lim, Poisoning effects of H_2S and HCl on the naphthalene steam reforming and water-gas shift activities of Ni and Fe catalysts, *Fuel*, 2019, **241**, 1008–1018, DOI: 10.1016/j.fuel.2018.12.119.

56 H. J. Jung, S. J. Lee, R. Koutavarapu, S. K. Kim, H. C. Choi and M. Y. Choi, Enhanced Catalytic Dechlorination of 1,2-Dichlorobenzene Using Ni/Pd Bimetallic Nanoparticles Prepared by a Pulsed Laser Ablation in Liquid, *Catalysts*, 2018, **8**, 390, DOI: 10.3390/catal8090390.

57 X. Ma, Y.-X. Zhou, H. Liu, Y. Li and H.-L. Jiang, A MOF-derived Co–CoO@N-doped porous carbon for efficient tandem catalysis: dehydrogenation of ammonia borane and hydrogenation of nitro compounds, *Chem. Commun.*, 2016, **52**, 7719–7722, DOI: 10.1039/C6CC03149H.

58 L. Yate, L. Martínez-de-Olcoz, J. Esteve and A. Lousa, Ultra low nanowear in novel chromium/amorphous chromium carbide nanocomposite films, *Appl. Surf. Sci.*, 2017, **420**, 707–713, DOI: 10.1016/j.apsusc.2017.05.203.

59 S. Shi, X. Zhou, W. Chen, M. Chen, T. Nguyen, X. Wang and W. Zhang, Improvement of structure and electrical conductivity of activated carbon by catalytic graphitization using N2 plasma pretreatment and iron(III) loading, *RSC Adv.*, 2017, **7**, 44632–44638, DOI: 10.1039/C7RA07328C.

60 T. Borowiecki, W. Gac and A. Denis, Effects of small MoO_3 additions on the properties of nickel catalysts for the steam reforming of hydrocarbons: III. Reduction of Ni-Mo/Al_2O_3 catalysts, *Appl. Catal., A*, 2004, **270**, 27–36, DOI: 10.1016/j.apcata.2004.03.044.

61 X. Su, J. Xu, B. Liang, H. Duan, B. Hou and Y. Huang, Catalytic carbon dioxide hydrogenation to methane: a review of recent studies, *J. Energy Chem.*, 2016, **25**, 553–565, DOI: 10.1016/j.jechem.2016.03.009.

62 S. Rönsch, J. Schneider, S. Matthischke, M. Schlüter, M. Götz, J. Lefebvre, P. Prabhakaran and S. Bajohr, Review on methanation – from fundamentals to current projects, *Fuel*, 2016, **166**, 276–296, DOI: 10.1016/j.fuel.2015.10.111.

63 P. Frontera, A. Macario, M. Ferraro and P. Antonucci, Supported Catalysts for CO_2 Methanation: A Review, *Catalysts*, 2017, **7**, 59, DOI: 10.3390/catal7020059.

64 H. Wang, Z. Li, E. Wang, C. Lin, Y. Shang, G. Ding, X. Ma, S. Qin and Q. Sun, Effect of composite supports on the methanation activity of Co-Mo-based sulphur-resistant catalysts, *J. Nat. Gas Chem.*, 2012, **21**, 767–773, DOI: 10.1016/S1003-9953(11)60430-1.

65 B. Alrafei, I. Polaert, A. Ledoux and F. Azzolina-Jury, Remarkably stable and efficient Ni and Ni-Co catalysts for CO_2 methanation, *Catal. Today*, 2019, DOI: 10.1016/j.cattod.2019.03.026.

66 S. S. Maluf and E. M. Assaf, Ni catalysts with Mo promoter for methane steam reforming, *Fuel*, 2009, **88**, 1547–1553, DOI: 10.1016/j.fuel.2009.03.025.

67 Q. Liu, Z. Zhong, F. Gu, X. Wang, X. Lu, H. Li, G. Xu and F. Su, CO methanation on ordered mesoporous Ni–Cr–Al catalysts: Effects of the catalyst structure and Cr promoter on the catalytic properties, *J. Catal.*, 2016, **337**, 221–232, DOI: 10.1016/j.jcat.2016.01.023.

68 M. A. A. Aziz, A. A. Jalil, S. Triwahyono and M. W. A. Saad, CO_2 methanation over Ni-promoted mesostructured silica nanoparticles: influence of Ni loading and water vapor on activity and response surface methodology studies, *Chem. Eng. J.*, 2015, **260**, 757–764, DOI: 10.1016/j.cej.2014.09.031.

